PCCP

Accepted Manuscript

ROYAL SOCIETY OF CHEMISTRY

www.rsc.org/pccp

Insights into reaction mechanism of CO oxidative coupling to dimethyl oxalate over palladium: A combined DFT and IR study

Qiaohong Li[a], Zhangfeng Zhou[a,b], Ruiping Chen[a], Baozhen Sun[a,c], Luyang Qiao[a,b], Yuangen Yao[*a,b], Kechen Wu[**a]

[a]*State Key Laboratory of Structural Chemistry, Key Laboratory of Coal to Ethylene Fujian Institute of Research on the Structure of Matter, Chinese Academy of Sciences, Fuzhou 350002, PR China*
[b]*Glycol and Its Related Technology, Fujian Institute of Research on the Structure of Matter, Chinese Academy of Sciences, Fuzhou 350002, PR China*
[c]*School of Chemistry and Chemical Engineering, Guangxi University, Nanning 53000 4, PR China*

ABSTRACT

The toxic pollutant CO could undergo oxidative coupling to the foundational raw chemical material Dimethyl Oxalate (DMO), which has been industrialized but the catalytic mechanism has been unknown so far. The reaction mechanism of CO oxidative coupling to DMO on a Pd(111) surface has been investigated using density functional theory (DFT) and *in situ* diffuse reflectance infrared (DRIR) spectroscopy. DFT calculations and *in situ* DRIRS measurements indicate that two co-adsorbed intermediates COOMe and OCCO, initiate the reaction. C-C coupling occurs earlier due to a low coupling barrier and small steric hindrance. The results also suggest that a Pd(111) is selective for DMO over DMC, and CO pre-adsorption and excessiveness effectively enhance the yield of DMO. The microscopic elucidation of this important reaction suggests the following improvements in the coal-to-EG (CTEG) production

* Corresponding author. Fax: +86 591 83714946.
E-mail address: yyg@fjirsm.ac.cn (Y. Yao).
** Corresponding author. Fax: +86 591 83792932.
E-mail address: wkc@fjirsm.ac.cn (K. Wu).

which have been applied in practice, effectively enhancing the yield and reducing the cost. The results may help with the further fine-designing of high-efficient noble metal catalysts.

Keywords: carbon oxide, dimethyl oxalate, palladium, DFT, *in situ* DRIRS

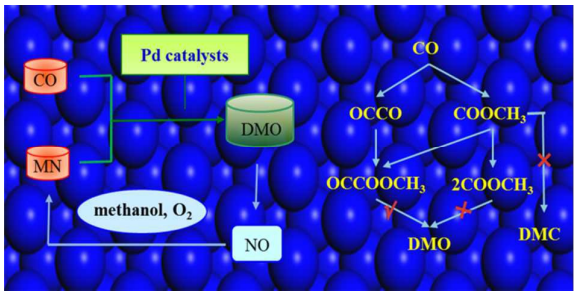

1. Introduction

Industrial exhaust gas (IEG) contains large amounts of CO, and most of the tail gas is burned and no longer used. How to reuse tail gas, particularly CO. It is highly an important topic. If the tail gas after purification can be used to synthesize carbon chemical products, this use will not only avoid the greenhouse effect due to CO combustion and emission of CO_2, but will also reduce the production cost and generate economic benefits, combining high additional value resources with energy and environmental protection, promoting sustainable development in the chemical industry. Due to modern economic construction and social activities, the requirements for energy and synthetic materials are increasing. Energy crisis aggravate the embarrassing situation of chemical raw material shortage. The development of the natural gas- and coal-based carbon chemical industry has become an important bridge between the coal chemical industry, natural gas and the petrochemical industry. Most recently, a lower-cost preparation of EG called to coal-to-EG pathway (CTEG) has been successfully developed and industrialized[1-7].

Dimethyl oxalate [$(COOCH_3)_2$, DMO] is a foundational raw chemical material. For example, the hydrogenation of DMO forms ethylene glycol [$(CH_2OH)_2$, EG], of which more than 25 million tons is produced every year worldwide. One of the most important reaction steps is CO oxidative coupling to form DMO on palladium-based heterogeneous catalysts, in which inorganic C1 (CO) is converted to organic C2 (DMO) [8, 9]. The reaction equation has been given as below:

$$2CH_3NO_2 + 2CO \xrightarrow{Pd} (COOCH_3)_2 + 2NO \qquad (1)$$

(MN) (DMO)

This route is environmentally friendly, as the toxic pollutant CO react to form DMO and NO, and the toxic pollutant NO can then be reused with O_2 to produce MN.

CO oxidation has been extensively investigated in the past 40 years, and a number of noble metals (e.g., Pt, Au, Ir, Pd, Cu)[10-20] and metal oxides[21, 22] have been identified as active catalysts for CO oxidation. Nano Pd-based heterogeneous catalysts have been demonstrated to be active for CO oxidative coupling to DMO [23]. A variety of experimental techniques including infrared reflection-adsorption spectroscopy (IRAS)[24], low energy electron diffraction (LEED)[25], photoelectron diffraction[26], high-resolution core level spectroscopy (HRCLS)[27], and scanning tunneling microscopy (STM)[28], as well as theoretical calculations[29, 30] have been employed to study the system of CO on the Pd(111) surface. However, the structure-reactivity relationship in CO oxidation with MN coupling to DMO has been unknown so far.

For a long time, the catalytic mechanism of Eq. 1 has been open to debate. Waller[31] has proposed a conjectural mechanism for the di-alkyl oxalate by an intramolecular coupling reaction. It has been speculated that MN oxidises Pd to generate an intermediate ON-Pd-OMe, and CO inserts to give ON-Pd-COOMe. Repeating the formation of the ON-Pd-COOMe leads to a Pd-$(COOMe)_2$ intermediate, and finally, a coupling reaction results in the formation of DMO. In addition, It has been proposed that a second CO insertion on ON-Pd-COOMe is possible, giving ON-Pd-CO (COOMe). S. Uchiumi[32] found that MN dissociative adsorption provides

Pd-OMe, as alcohol has no effect on the rate of the DMO formation. This work also notes that the catalytically active species for the formation of oxalated are Pd^0.

Subsequently, Xu et al[33] combined XPS and in situ DRIRS study of the mechanism of the Pd–Fe/α-Al_2O_3 catalysed CO coupling reaction to produce diethyl oxalate. They noted that two types of Pd^{2+} represent two intermediates, $Pd(OR)_2$ and $Pd(COOR)_2$. Yang[34] used in situ infrared spectroscopy to investigate the reaction and determined that the formation of DMO is initiated by MN adsorption and CO adsorption, resulting in two intermediates ON-Pd-OMe and ON-Pd-COOMe, ultimately coupled by two ON-Pd-COOMe intermediates. They still note that only bridge CO adsorption participates in the reaction.

Recently, the Guo research team[30] proposed an analogous mechanism, beginning with the formation of the intermediate 1 (MeO-Pd-OMe) followed by the insertion of CO into intermediate 1 to form MeOOC-Pd-COOMe and finally a rapid coupling reaction resulting in the formation of DMO. Their DFT calculation results showed that the linear absorption mode of CO on the Pd(111) facets is crucial for CO oxidative coupling to DMO.

Hence we can see the agreement that C-C coupling occurs in the last step by double carbonylation, except by Waller, who proposes the CO might couple with ON-Pd-COOR to form ON-Pd-CO (COOMe). At least two types of intermediates exist in the reaction process. However, the reaction pathways described above are based on inference, without sufficient evidence based on either experiments or calculations. In this study, we have examined the reaction pathway in which CO with

MN (initiation state, IS) undergoes oxidative coupling to DMO (final state, FS) through DFT computations as well as *in situ* diffuse reflectance infrared spectroscopy (in situ DRIRS), transmission electron microscopy (TEM), high resolution TEM (HRTEM), and X-ray photoelectron spectroscopy (XPS). Understanding the CO oxidative coupling mechanism on Pd catalyst in the CTEG process will significantly benefit the improvement of the CTEG production in both high-yield and low-cost.

Palladium catalyst has been reported to be effective for Eq.1[9, 23, 35-37], and the (111) facet has been identified as the active plane in catalysis[30]. The binding of the molecular reactants and inter-reactants (CO, NO, OMe and MN) on the Pd(111) surface ensures the reaction in Eq.1. The stable adsorptions of CO, NO and OMe on the Pd(111) surface have already been reported [30, 38-40]. The most favourable adsorption sites are the *fcc* sites on the Pd(111) surface. Consequently, a systematic calculation of the adsorption of both CO and MN on a perfect Pd(111) surface was been performed before the study of the oxidative coupling reaction.

2. Experimental

2.1 DFT study

As an inert carrier, the effect of α-Al_2O_3 is not considered in this study. Fig.1S shows the Pd(111) perfect surface represented by five layer slabs with a p(√3*√3) supercell. Without the adsorbate, the vacuum between the slabs is set to span a range of 15 Å. All atoms of the two bottom layers are fixed to the bulk positions. The adsorbate is set on one side of the slab. In Fig.1S several adsorption sites are indicated, and a detailed account of these adsorption sites is given.

All calculations are performed according to the density functional theory (DFT) approach using the Dmol^3 software package[41, 42], which can simulate periodic systems. The generalized gradient approximation (GGA) is adopted to describe the density functional using the Perdew-Burke-Ernzerhof (PBE)[43, 44] functionals for the exchange-correlation term. The reliability of the method has been confirmed by previous reports regarding the absorption on Pd surface[45-48]. The wave functions are expanded in terms of numerical basis sets. The double-numeric quality basis set with polarisation functions (DNP[41, 49, 50]) is adopted which is comparable to 6-31G**[51-53]. The numerical basis sets can minimise the basis set superposition error[54]. All-electron basis sets are performed for all the elements except Pd, which is treated using the effective core potential. A Fermi smearing of 0.005 hartreeis utilized, and Brillounin zone integration is set to 3×3×1. The tolerances of the energy, gradient and displacement convergence are 1×10^{-5}hartree, 2×10^{-3}hartree/Å, 5×10^{-3}Å, respectively. The transition states (TS) are located using the complete linear synchronous transit/quadratic synchronous transit (LST/QST) methods. First, LST maximization is performed, followed by a reaction pathway. The TS approximation obtained in this way is used to perform QST maximisation. From that point, another conjugate gradient minimisation is performed. The cycle is repeated until a stationary point is located.

The adsorption energies ΔE_{ads} are defined as follows,

$$\Delta E_{ads} = E_{total} - [E_{slab} + E_{adsorbate}]$$

where E_{total} represents the total energy for the slabs with adsorbate. E_{slab} represents the

total energy of the bare slab of the surface. $E_{adsorbate}$ represents the totalenergies of free adsorbate molecules.

The interaction energies (ΔE_{int}) and the energies of the co-adsorption of two molecules A and B ($\Delta E_{co\text{-}ads}$) were calculated, as follows

$$\Delta E_{int} = E_{ads,\ A+B} - E(A) - E(B)$$

$$\Delta E_{co\text{-}ads} = E_{total} - [E_{slab} + E(A) + E(B)] - \Delta E_{int}$$

where $E_{ads,\ A+B}$ represents the total energy of two free adsorbate molecules (A+B) being co-adsorbed. E(A or B) represents the total energies of free adsorbate molecules A or B.

2.2. Catalyst preparation and characterisation

The Pd/α-Al_2O_3(1.5 wt.% Pd) catalyst is prepared by wet impregnation of $PdCl_2$ (AR, Sino-Platinum Co., Ltd., China) in diluted hydrochloric acid solution and is dried at 423K for 24 h then calcined in air at 673K for 12 h. Before the prepared catalyst is used, it must be reduced in hydrogen at 453K for 12 h.

Samples for transmission electron microscopy (TEM) and high-resolution TEM (HRTEM) observations are prepared by drying a drop of diluted ethanol dispersion of Pd/α-Al_2O_3 catalyst on acopper grid. Particle sizes and shapes are examined by a TEM (JEM-2010) operated at 200 kV, equipped with a Gatan-794-MSC CCD camera system, a Gatan-676TV system, and an OXFORD-INCA ultra-thin window EDS system.

X-ray photoelectron spectroscopy (XPS) data are obtained using a VG MultiLab 2000 analyser with a Mg $K\alpha$ radiation source and the binding energies are referenced

to C 1*s* (284.6 eV).

The *in situ* diffuse reflectance infrared spectroscopy (DRDIRS) measurements are performed on a Nicolet 6700 Fourier transform infrared spectrometer equipped with a stainless steel *in situ* IR flow cell. The powder samples are placed into the cell after pre-treat in N_2 flow for 30 minutes at 423 K. After the samples are reduced in H_2 flow at 453 K for 3 h and cooled to the desired temperature, a reference spectrum is recorded. Then, the reactants are introduced in constant flow, and the spectra are recorded at a resolution of 4 cm^{-1} for 64 scans.

2.3 Activity test and product analysis

The activities of the Pd/α-Al_2O_3 catalysts for CO oxidative coupling to DMO are evaluated in a fixed-bed glass tubular reactor. The Pd/α-Al_2O_3 catalysts (1 g) are placed in the reactor and reduced in a H_2 atmosphere at 453 K for 12 h with a ramp rate of 2 K/min from room temperature, a H_2 flow rate of 30 ml/min, and a pressure of 0.12 MPa. After cooling to room temperature with N_2 flow, the reactant gases (CO, MN, and N_2balance) are passed through the reactor at a gas hourly space velocity (GHSV) of 3000 h^{-1} with a ramp rate of 2 K/min from room temperature to reaction temperature under a pressure of 0.12 MPa. The products are condensed and analysed by an Agilent GC-7820A gas chromatograph fitted with a flame ionisation detector.

The space-time yield of DMO is calculated using the following formula: STY of DMO ($gL^{-1}h^{-1}$) = Weight of DMO g/ (Volume of the catalyst × Reaction time L·h)

3. Results and discussion

3.1 Complexes of Pd(111) with CO or MN

The reaction begins with the adsorption of CO and MN molecules over the Pd(111) surface. CO binds to the Pd(111) surface in four modes (*i.e.,* the *top, bridge, hcp,* and *fcc* modes) with the carbon atom approaching the surface. The most favourable adsorption site is the *fcc* site. The results agree well to the previous[30, 38-40, 55] reports.

For the MN molecule, *cis*-mode is reported to be more stable than *trans*-MN in both theoretical and experimental reports[56-61]. The parallel adsorption and vertical adsorption of an *cis*-MN molecule on the four sites of the Pd(111) surface (16 models) are tested. Dissociative adsorption is most likely type of adsorption on the surface. Due to the small N-O bond energy (42 kcal/mol[62]), the N-O bond is easy to break, and as consequence MN can be dissociated into the OMe radical molecule, which initiates the reaction of CO oxidative coupling to DMO.

3.2 Stable intermediates adsorption on Pd(111)

To map out the mechanism of CO oxidative coupling to DMO, the co-adsorption of CO+OMe and CO+CO have been studied. After testing different possible co-adsorption configurations, interestingly, we found the stable configurations COOMe and OCCO, respectively. Compared with individual adsorption, for the COOMe compounds shown in Fig. 1, the C1-O1 is slightly activated: the bond length increase from 1.141 to 1.214 Å, and the new C1-O2 bond (1.359 Å) is formed, finally leading to the formation of COOMe.

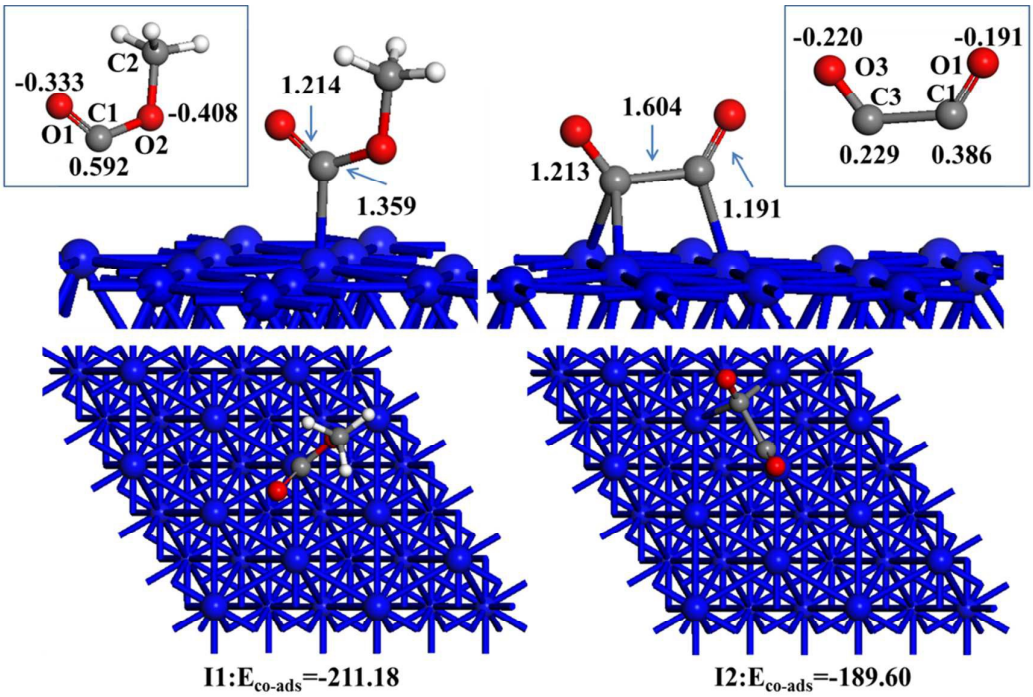

Fig. 1 The optimised stable intermediates formed by CO + OMe and CO + CO co-adsorption on Pd(111). I1: COOMe species; I2: OCCO species. The values in the blue rectangles indicate Mulliken charges. The bond lengths and the adsorption energies are given in Angstroms and kcal/mol. The blue, grey, red, and white balls denote Pd, C, O and H atoms, respectively. The same colour scheme is applied in **Figs. 5-7**.

For OCCO compounds, the C-O is also slightly activated: the bond length increase from 1.151 to 1.191 and 1.213 Å, and the new C-C (1.604 Å) is formed. In particular, their adsorption energies are -211.18 and -189.60kcal/mol, respectively. The large adsorption energies clearly suggest the stability of COOMe and OCCO complexes on Pd(111). In addition, according to the atomic charges shown in Fig. 1, the C1 and O2 atoms (for COOMe) of the newly formed C-O bond attract each other, and the electrostatic interaction further enhances the stability of the COOMe intermediate. For OCCO, although the C atoms of the newly formed C-C bond repel each other, the Pd stabilises the OCCO by back-donation interaction because the calculated charges of the Pd surface have a negative charge.

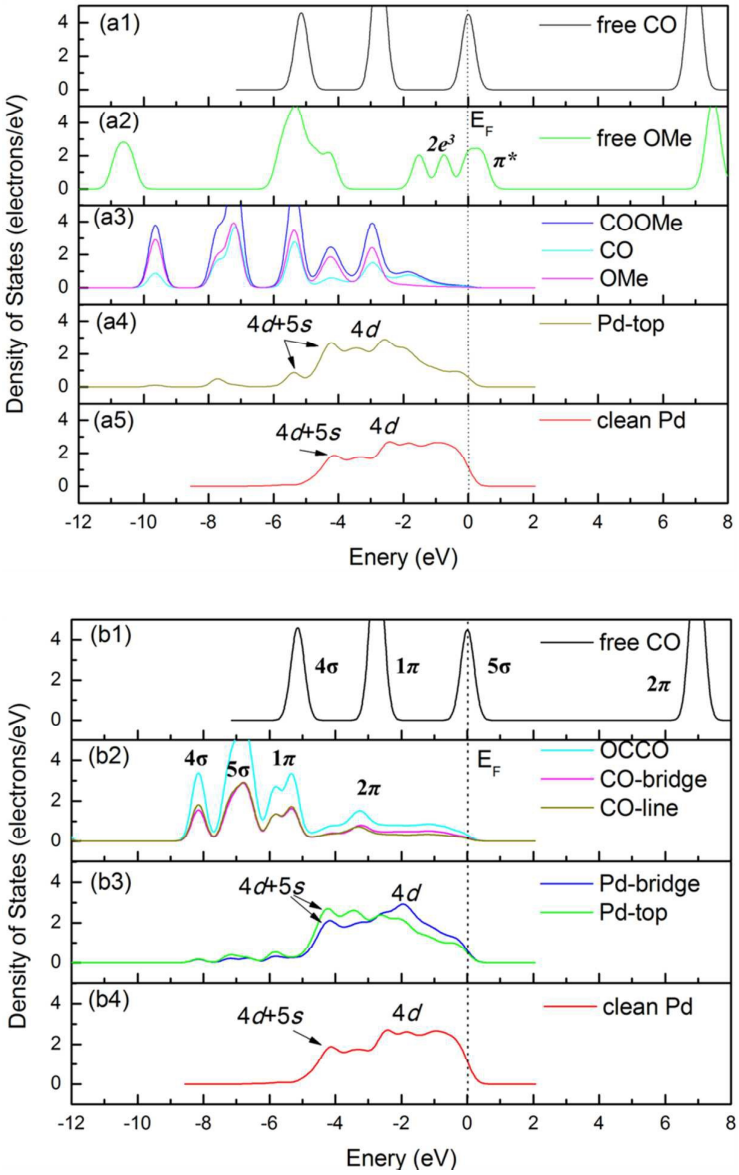

Fig. 2 DOS of separated components (CO, OMe, and Pd, respectively) before and after adsorption. (a) for I1; (b) for I2.

The density of states (DOS) on the separated components (adsorbates and Pd, respectively) in the absorbed COOMe and OCCO configuration are given in Fig. 2. For the COOMe compound, the partial density of states (PDOS) plot shown in Fig. 2A (a3) and (a4) clearly show that a strong C1-O2 bond between CO and OMe is

formed, as indicated by significant overlaps between the CO 2π and OMe 2e^3+π* orbitals. In addition, to Pd(4*d*)-CO(2π) interaction, another important Pd(4*d*)-OMe(2e^3+π*) interaction is observed. For the OCCO compound, in the partial density of states (PDOS) plot shown in Fig.2B (b2) and (b3), there is a broadening of CO 2π overlap with the Pd 4*d* state (Pd(4*d*)-CO(2π)), suggesting that the electrons in Pd 4*d* orbital are transferred to the CO molecule, causing the two C=O bonds to elongate. The charge transfer back donates from CO to Pd because the calculated charges of the Pd surface have a negative charge. Meanwhile, there is good 2π overlap of bridge-CO and top-CO (CO(2π)-CO(2π)), leading to the formation of a new C-C bond between two CO molecules. Compared with the absorption of CO, the C=O stretching vibration peak of OCCO will redshift. Further comparing Figs. 2(a4) and (b3) shows that the Pd peaks in the COOMe complex shift to a the lower energy region than the ones in OCCO, indicating that the charge transfer between Pd and the adsorbates COOMe is stronger than OCCO. Combining the results on adsorption energies, electrostatic interaction and PDOS, it shown that COOMe and OCCO are stable on Pd(111), and COOMe is more stable than OCCO.

3.3 In situ DRIR measurements

In-situ infrared spectra are acquired after reactants have been injected into reaction cell, and reaction temperature has been set to the specified point. Fig. 3 shows the *in situ* DRIR spectra of CO adsorbed on the Pd/α-Al_2O_3 catalyst at 303, 363, 383, and 403 K, respectively. The bands at approximately 2170 and 2120 cm^{-1} are assigned to CO in gaseous phase, the peak at approximately 2080 cm^{-1} is assigned to linearly bonded

CO, and the adsorptions at approximately 1973 and 1942 cm^{-1} are assigned to bridge bonded CO[63, 64]. It is worth noting that certain peaks from 1750 to 1850 cm^{-1}, which are carbonyl peaks of some groups, respond to changes in temperature.

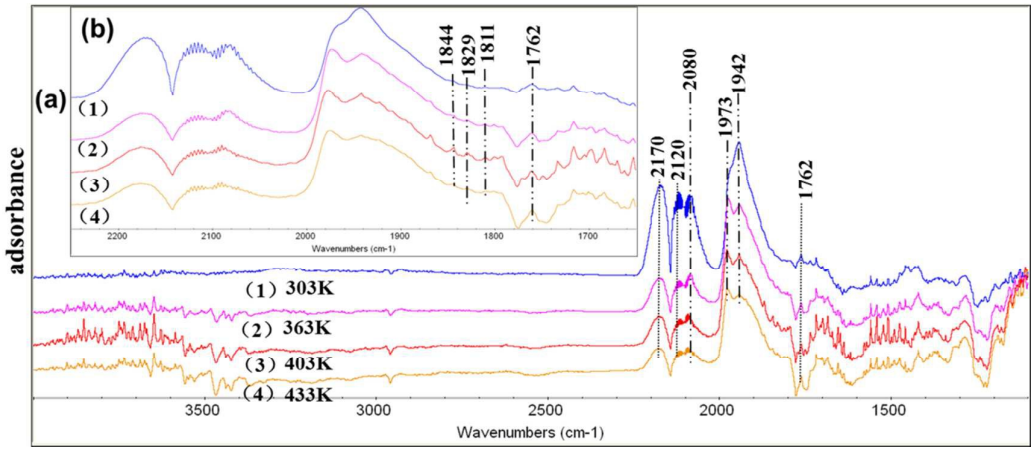

Fig. 3 (a) IR spectra of CO adsorption on Pd/α-Al_2O_3 at different temperatures; **(b)** CO adsorption of segment of (a). (1)303 K, (2)363 K, (3)403 K, (4)433 K. All *In situ* infrared acquisition data are first past into the gas, and temperature reach to the specified temperature after balance after 10 min data acquisition.

The bands at approximately 1844, 1829, 1811 (linearly adsorption CO of OCCO) and 1762 cm^{-1}(bridge adsorption CO of OCCO) could be attributed to OCCO[65-69]. Due to interaction between (Pd(4*d*)-CO(2π)) and (CO(2π)-CO(2π)), the C=O bond of OCCO is longer than the C=O bond of the individually adsorbed CO, and the C=O stretching vibrations peak of OCCO is redshiftsed. The peaks (approximately 1844, 1829, 1811 and 1762 cm^{-1}) of the intermediate O=C-C=O appear at 303 K, gradually increasing as the temperature rise from 303 K to 363 K and then to 403K, but gradually decreasing as the temperature rises further from 403 K to 433 K, indicating that the intermediate of O=C-C=O is easily formed from CO on the Pd catalyst, especially in the optimum reaction temperature range from 363 K to 433 K.

From Fig. 4(b), the absorbance at 1754 cm^{-1} could be referenced to the C=O

stretching vibration in the intermediate of COOMe, and the absorbance at 1778 and 1745 cm^{-1} could be referenced to the C=O stretching vibration in the intermediate of OCCOOMe, for the conjugate effect of the OMe group in OCCOOMe that cause the

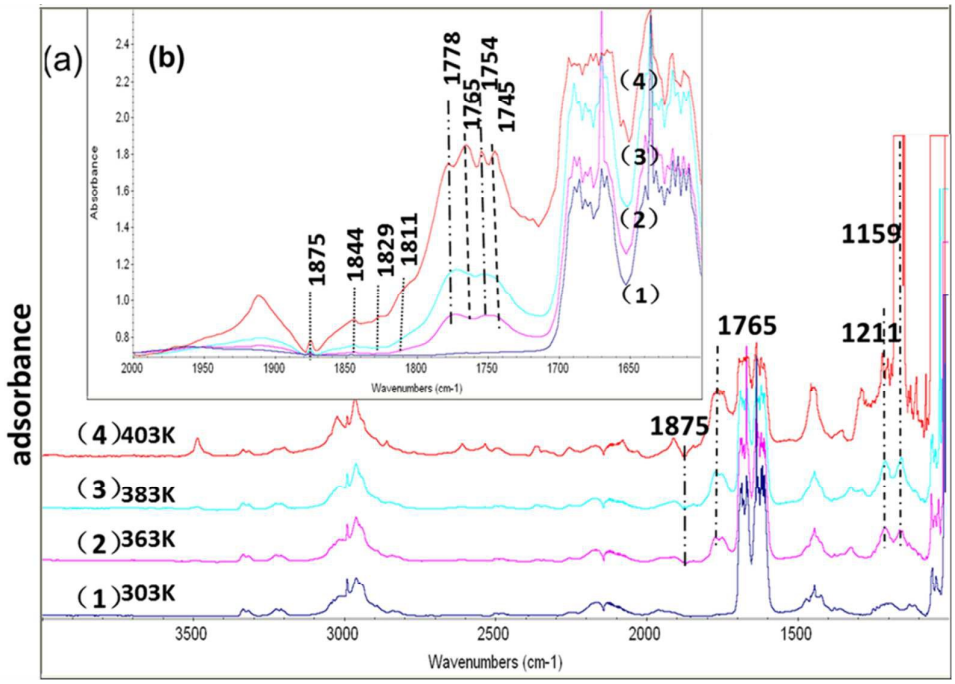

Fig. 4 (a) IR spectra of CO and MN coupling reaction after CO pre-adsorption on Pd/α-Al_2O_3 at different temperatures; (**b**) CO and MN coupling reaction of segment of (**a**) on the same scale. (1)303 K, (2)363 K, (3)383 K, (4)403 K. All *In situ* infrared acquisition data are first past into the gas, and temperature reach to the specified temperature after balance after 10 min data acquisition.

absorbance to red shift from 1844, 1829, 1811 and 1762 cm^{-1} of the intermediate OCCO. Clearly, the C=O stretching vibration peak from CO to OCCO to COOMe to OCCOOMe is a gradual redshift process.

Fig. 4(a) shows *in situ* DRIR spectra of the CO and MN coupling reaction after CO pre-adsorption on Pd at 303, 363, 383 and 403 K, respectively. The band at approximately 1875 cm^{-1} is assigned to gaseous NO of the product, the bands at approximately 1765 cm^{-1} are assigned to the C=O stretching vibrations, and the bands

at approximately 1211 and 1159 cm^{-1} are assigned to the C-O stretching vibrations of the product, DMO[70]. Moreover, all the peaks gradually increase from 363 K to 403 K. In addition, Fig. 4 shows a few characteristic vibration bands (1298 cm^{-1}) of dimethyl carbonate (DMC)[71].

3.4 Reaction profiles for CO oxidation coupling to DMO

On the basis of adsorption results, CO oxidation to DMO on Pd (111) has been studied. Because N-O bond is easy to break, MN can be dissociated

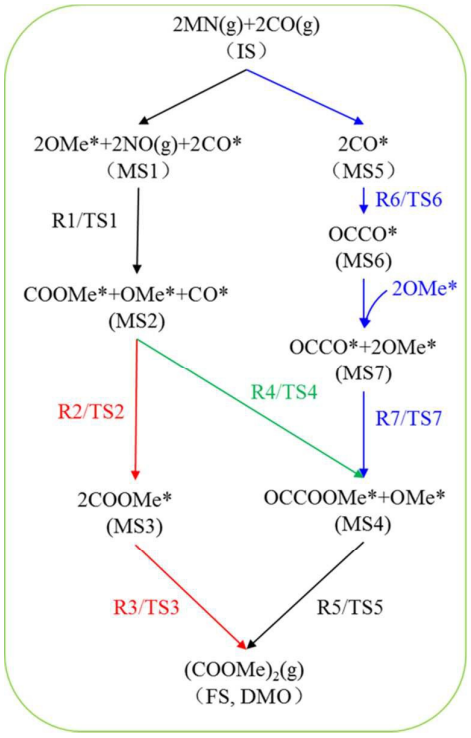

Schema 1 The pathway network for the reaction of CO and MN. P1 (red, C-C coupling occurs in the third step), P2 (green, C-C coupling occurs in the second step), and P3 (blue, C-C coupling occurs in the first step)

into the OMe radical, and the intermediate state (MS) of 2OMe*+2CO* initiates the reaction of CO oxidative coupling to DMO, whose initiation state (IS) is 2 MN and 2 CO. Three different pathways for CO oxidation to DMO have been considered in the present work as shown in schema1 and Figs. 5-7. All of the geometries of minima and

transition states (TS) along each path are provided to describe the reaction processes clearly.

3.4.1 Profiles for P1

P1:R1→R2→R3

As shown in Fig. 5, P1 begin with the co-adsorptions of CO, and OMe on Pd(111) (intermediate state, MS1). The adsorbed OMe molecule obliquely binds onto the surface in a configuration such that O binds to a *top* site. It then approaches the carbon of the nearby adsorbed CO through its oxygen to form a highly stable intermediate complex (COOMe, MS2) via a transition state (TS1).

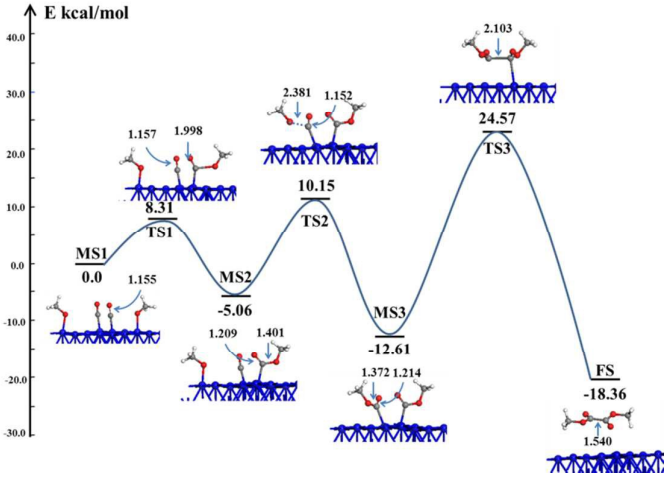

Fig.5 The energy profile (P1) for the reaction of CO and MN. All energies are given in kcal/mol.

This process is accompanied first by heat absorption of 8.31 kcal/mol and then, from TS1 to MS2, heat releases of 13.37 kcal/mol. The other COOMe is formed along MS2-TS2-MS3, which is exothermic (7.55 kcal/mol) with a small barrier of 15.21 kcal/mol, finally leading to the formation of two COOMe (intermediate state, MS3). The following coupling process of MS3 on the Pd surface must surmount a high energy barrier via a transition state (TS3) with the endothermic heat of 37.18 kcal/mol

and is exothermic by 5.75kcal/mol to FS (DMO). A high energy barrier (TS3) must be overcome due to the formation of the new C-C, electrostatic interaction, and steric effect. The calculated results strongly suggest that in P1, the C-C coupling (overpass TS3 peak) is extremely difficult. From the structure analysis, along the reaction coordinate, first the two new C-O bonds (1.401 and 1.372 Å) of CO and OMe areformed, respectively, leading to the formation of two COOMe intermediates and then, finally, the formation of new C-C bond between two COOMe molecules, accompanied by the decomposition of DMO. Many experimental scientists[30, 31, 33, 34, 63] have proposed the catalytic mechanism of CO oxidation to DMO through coupling with two COOMe complexes, which is not feasible according to our DFT calculation results.

3.4.2Profile of P2

P2:R1→R4→R5

As shown in Fig. 6, P2 also begins with the co-adsorptions of reactants on the Pd(111) surface (MS1). The first reaction step is the same as P1. In the second step, COOMe attacks CO to form an intermediate complex (OCCOOMe, MS4).in the last step, OMe approaches the carbon of OCCOOMe to form DMO. The reaction pathway diagram in Fig. 6 shows that the C-C coupling is from MS2 to MS4, accompanied by endothermic heat of 2.55 kcal/mol with a moderate barrier by 28.31 kcal/mol (TS4), and the formation of DMO with OCCOOMe and OMe must overcome a moderate barrier of 27.39 kcal/mol and is exothermic (15.85 kcal/mol). The barriers involved in the two steps are not insurmountable. Compared with P1, for P2, the C-C coupling

reaction barrier lowers because the formation of C-C with COOMe and CO must overcome lesser electrostatic interaction and steric effect. Consequently, pathway P2 is favourable to towards Eq.1.

In addition, due to the co-existence of CO and OMe, the pathway for CO oxidation to dimethyl carbonate (MeOCOOMe, DMC) in Pd(111) has also been considered (Fig. 6). The formation of DMC with COOMe and OMe must overcome a high barrier of 47.38 kcal/mol and is exothermic (32.21 kcal/mol). It is very difficult for CO oxidation to DMC to occur on Pd(111), which is consistent with the results of*in situ* DRIR spectra and space-time yield results.

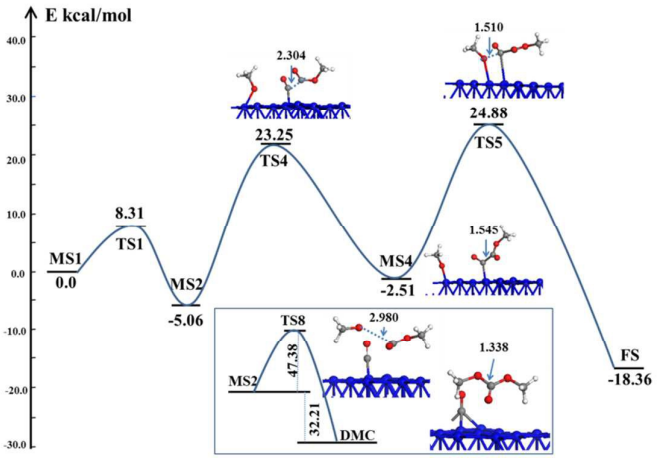

Fig.6 The energy profile (P2) for the reaction of CO and MN. All energies are given in kcal/mol.

For CO oxidation to DMO, the highest reaction energy is required to overcome the coupling of C-C in both proposed pathways of P1 and P2. The reason may lie in the large steric hindrance of the COOMe intermediates, in which OMe fragment blocks the C-C coupling. If C-C coupling occurs before the formation of the OMe fragment the steric effect may be reduced. With this idea in mind, we suggest a new reaction pathway (P3), in which two adsorbed CO molecules couple together to form

an OCCO fragment before the COOMe coupling process.

3.4.3 Profile of P3

P3: R6→R7→R5

As shown in Fig.7, P3 begins with the co-adsorption of two CO molecules on

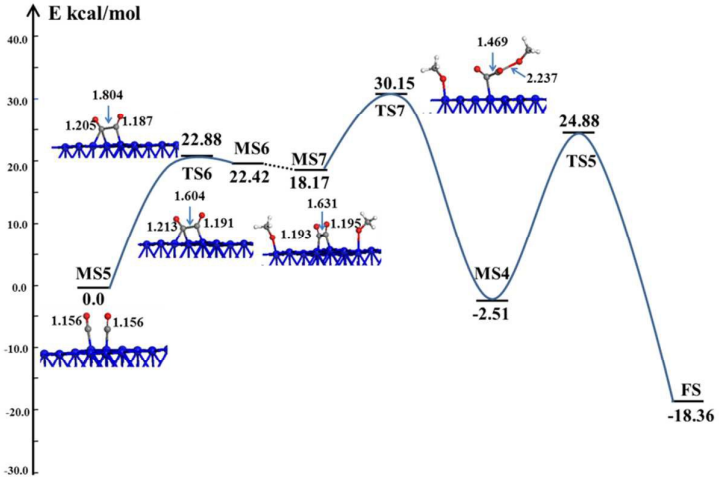

Fig. 7. The energy profile (P3) for the reaction of CO and MN. All energies are given in kcal/mol.

Pd(111) (intermediate state, MS5), and then the two OMe molecules approach the two carbon atoms of OCCO in turn to finally form DMO. Fig. 7 shows two CO molecules coupled to each other to form OCCO intermediate (MS6) via the transition state TS6. This process is accompanied by a moderate barrier of 22.88 kcal/mol (TS6) and an endothermic heat of 22.42 kcal/mol. Based on the adsorption energies, PDOS and *in situ* DRIR, the results show that OCCO is stable on Pd(111). Significantly, the energy of MS6 is only lower (0.46 kcal/mol) than TS6. The reaction $2CO \leftrightarrow OCCO$ is reversible. We suppose that when CO is pre-adsorption and in excess, the reaction is able to proceed to the right, as shown by the results of *in situ* DRIR spectra. Then, the OMe molecules can attack one carbon atom of OCCO to form OCCOOMe, and the

process is exothermic (20.68 kacl/mol) surmounting the energy barrier (TS7, 11.98 kacl/mol). Finally, the other OMe approaches and binds through its oxygen to the adsorbed OCCOOMe via TS5, which is the same as the third step of P2. Accordingly we suggest that P3 with CO pre-adsorbed and in excess is a feasible reaction path of CO oxidative coupling to DMO on the Pd(111) surface.

Table 1

Effect of reaction temperature on space-time yield of DMO.(3000 h^{-1},30% CO, 20% MN, and N_2 balance).

Reaction temperature (K)	Yield of DMO (g/L.h)	Selected o DMO(%)	Selected of DMC(%)
363	60	100	0
373	240	99.9	0.1
383	420	99.9	0.1
393	710	99.8	0.2
403	860	99.6	0.4
413	790	99.6	0.4
423	680	99.5	0.5
433	460	99.5	0.5

According to the above results, it is clear that the mechanism of CO oxidation on Pd(111) differs from the former proposed mechanism, which first form the complex of two COOMe intermediates followed by the coupling of two COOMe to form DMO. It is obvious that the C-C coupling step is crucial. Our calculated results reveal that there are three steps for CO oxidation on Pd(111), that C-C coupling happens earlier before the formation of OMe fragment, and that the energy barrier is lower. When CO oxidation to DMO occurs along the P1 pathway, it is easy to form COOMe, but is difficult to accomplish coupling of the two COOMe intermediates. Our transition state

calculations clearly reveal that pathways P2 and P3 are both viable. However, for P3, OCCO is decomposed to adsorbed CO. We know that when CO is pre-adsorpted and in excess, the reaction (2CO ↔ OCCO) is able to proceed to the right. In this view, our experimental results reflect the influence of molar ratio of CO to MN on the space-time yield of DMO at 403K (3000 h^{-1}, 50% N_2 balance, 0.12 MPa)

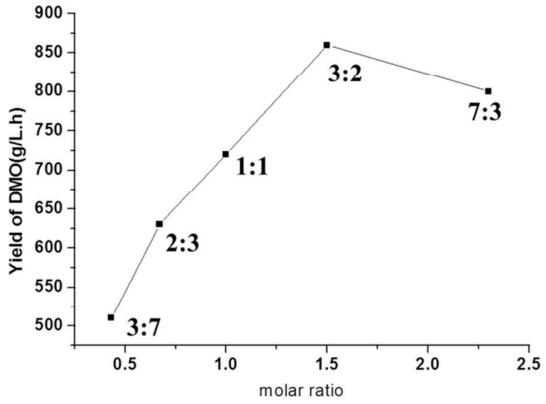

Fig. 8. Influence of molar ratio of CO to MN on space-time yield of DMO at 403K. (3000 h^{-1}, 50 % N_2 balance, 0.12 MPa)

shown in Fig. 8, and the effect of reaction temperature and ventilation order of CO and MN in Table 1 and 2. We conclude that the oxidation of MN and CO on Pd(111) catalysts is most selective for DMO at different temperature, and the space-time yield of DMO can reach 99.5%, as in the DFT calculations. In addition, the results also suggest that for the reaction of CO and MN to DMO, CO pre-adsorption is best, and the best molar ratio of the reactants CO and MN is 3:2 (CO excess). For the molar ratio of the reactants CO and MN, when CO was excessive in the molar ratio of reactants CO and MN, it was conducive to occurrences of intermediate OC-CO

coupling of carbon monoxide and intermediate COOMe. However, the overdosed CO could lead to the shortage of OMe, which would be formed to DMO with intermediates OC-CO and OC-COOMe. It can be concluded from experiments that the ratio of reactants CO: MN at 7:3 would have lower yield of DMO than that of 3:2.

Table 2

Effect of reaction condition on space-time yield of DMO at 403K (3000 h^{-1}, 30 % CO, 20 % MN, and N_2 balance, 0.12 MPa,). Reaction condition: 1, CO pre-adsorption for 10 minutes; 2, introducing CO, MN at the same time; 3, MN pre-adsorption for 10 minutes. Reaction time：2 hours.

ventilation sequence	1	2	3
Yield of DMO (g/L.h)	860	780	650

4. Conclusions

In summary, the chemical reaction mechanism of CO oxidative coupling to DMO on a Pd(111) surface has been studied within the DFT computational framework as well as by *in situ* DRIRS measurements. The key point step is the C-C coupling, and CO oxidative coupling occurs in the first step of the reaction to form the OCCO intermediate over Pd(111) to reduce the steric hindrance in the coupling, but OCCO is easily decomposed. Our experimental results showed that when CO is pre-adsored and in excess, the reaction (2CO ↔ OCCO) is able to proceed to the right. Thus, the pathway along P3 is viable under certain conditions. Of course, in this case, the pathway P2, which first forms the highly stable COOMe intermediate followed by the C-C coupling in the second step, seems to perform best, as the highest barrier is 28.31 kcal/mol and can be overcome. Nevertheless, we find that the formation of di-alkyl oxalate by double carbonylation (P1), which is widely suggested, is unfeasible due to

a large barrier (37.18 kcal/mol). In addition, we also found that Pd(111) is selective for DMO rather than DMC, and the space-time yield of DMO is up to 99.5%. In summary, our results reveal that Pd(111) can facilitate CO oxidation through different mechanisms and the pathways along P2 and P3 operates favourably. It is hoped that our theoretical and experimental work will provide instructive information for further exploration of the intriguing chemistry of CO oxidation and guidance of industrial production. The microscopic elucidation of this important reaction suggests improvements in CTEG production, which have been applied in practice effectively enhancing the yield and reducing the cost. The results may benefit by the further replacement of high-priced noble metal catalysts.

Acknowledgements

This work is supported by NSFC projects (Nos. 91122015, 21201165, 21171165 and 21303025), 973 Program of China (2011CBA00505) and FJPNSF project (2013J05040). We acknowledge the Supercomputing Centre of CNIC for providing the computer resources.

References

1. Z. F. Zhou, Z. J. Li, P. B. Pan, L. Lin, Y. Y. Qin and Y. G. Yao, *Chem. Ind. Eng. Prog.*, 2010, **29**, 2003-2009.
2. L. Lin, P. B. Pan, Z. F. Zhou, Z. J. Li, J. X. Yang, M. L. Sun and Y. G. Yao, *Chin. J. Catal.*, 2011, **32**, 957-969.
3. L.-F. Chen, P.-J. Guo, M.-H. Qiao, S.-R. Yan, H.-X. Li, W. Shen, H.-L. Xu and K.-N. Fan, *J. Catal.*, 2008, **257**, 172-180.
4. A. Y. Yin, X. Y. Guo, W. L. Dai and K. N. Fan, *Chem. Commun.*, 2010, **46**, 4348-4350.
5. J. D. Lin, X. Q. Zhao, Y. H. Cui, H. B. Zhang and D. W. Liao, *Chem. Commun.*, 2012, **48**,

1177-1179.

6. Z. He, H. Q. Lin, P. He and Y. Z. Yuan, *J. Catal.*, 2011, **277**, 54-63.
7. Y. N. Wang, X. P. Duan, J. W. Zheng, H. Q. Lin, Y. Z. Yuan, H. Ariga, S. Takakusagi and K. Asakura, *Catal. Sci. & Tech.*, 2012, **2**, 1637-1639.
8. D. M. Fenton and P. J. Steinwand, *J. Organ. Chem.*, 1974, **39**, 701-704.
9. X. G. Zhao, Q. Lin and W. D. Xiao, *Appl. Catal. A*, 2005, **284**, 253-257.
10. B. E. Nieuwenhuys, *Adv. Catal.*, 1999, **44**, 259-328.
11. J. Gustafson, R. Westerström, A. Mikkelsen, X. Torrelles, O. Balmes, N. Bovet, J. N. Andersen, C. Baddeley and E. Lundgren, *Phy. Rev. B*, 2008, **78**, 045423.
12. B. Qiao, A. Wang, X. Yang, L. F. Allard, Z. Jiang, Y. Cui, J. Liu, J. Li and T. Zhang, *Nat. Chem.*, 2011, **3**, 634-641.
13. Y.-G. Wang, Y. Yoon, V.-A. Glezakou, J. Li and R. Rousseau, *J. Am. Chem. Soc.*, 2013, **135**, 10673-10683.
14. M. Okumura, N. Masuyama, E. Konishi, S. Ichikawa and T. Akita, *J. Catal.*, 2002, **208**, 485-489.
15. S. D. Gardner, G. B. Hoflund, B. T. Upchurch, D. R. Schryer, E. J. Kielin and J. Schryer, *J. Catal.*, 1991, **129**, 114-120.
16. Y. Li, Y. Yu, J.-G. Wang, J. Song, Q. Li, M. Dong and C.-J. Liu, *Appl. Catal. B: Environ.*, 2012, **125**, 189-196.
17. K. Ruth, M. Hayes, R. Burch, S. Tsubota and M. Haruta, *Appl. Catal. B,*, 2000, **24**, 133-138.
18. X. Liu, Y. Sui, T. Duan, C. Meng and Y. Han, *Physical Chemistry Chemical Physics*, 2014.
19. X. Tang, J. Schneider, A. Dollinger, Y. Luo, A. Wörz, K. Judai, S. Abbet, Y. Kim, G. Ganteför and D. Fairbrother, *Physical Chemistry Chemical Physics*, 2014, **16**, 6735-6742.
20. S. Lin, X. Ye, R. S. Johnson and H. Guo, *The Journal of Physical Chemistry C*, 2013, **117**, 17319-17326.
21. S.-Y. Wang, N. Li, L.-F. Luo, W.-X. Huang, Z.-Y. Pu, Y.-J. Wang, G.-S. Hu, M.-F. Luo and J.-Q. Lu, *Applied Catalysis B: Environmental*, 2014, **144**, 325-332.
22. C. Tang, J. Sun, X. Yao, Y. Cao, L. Liu, C. Ge, F. Gao and L. Dong, *Applied Catalysis B: Environmental*, 2014, **146**, 201-212.
23. Y. Yamamoto, *Catal. Surv. Asia*, 2010, **14**, 103-110.
24. E. Ozensoy, D. C. Meier and D. W. Goodman, *J Phy. Chem. B*, 2002, **106**, 9367-9371.
25. H. Ohtani, M. Van Hove and G. Somorjai, *Surf. Sci.* , 1987, **187**, 372-386.
26. T. Gießel, O. Schaff, C. Hirschmugl, V. Fernandez, K.-M. Schindler, A. Theobald, S. Bao, R. Lindsay, W. Berndt and A. Bradshaw, *Surf. Sci.* , 1998, **406**, 90-102.
27. S. Surnev, M. Sock, M. Ramsey, F. Netzer, M. Wiklund, M. Borg and J. Andersen, *Surf. Sci.* , 2000, **470**, 171-185.
28. M. Rose, T. Mitsui, J. Dunphy, A. Borg, D. Ogletree, M. Salmeron and P. Sautet, *Surf. Sci.* , 2002, **512**, 48-60.
29. N. M. Martin, M. Van den Bossche, H. Grönbeck, C. Hakanoglu, F. Zhang, T. Li, J. Gustafson, J. F. Weaver and E. Lundgren, *J. Phys. Chem. C*, 2014, **118**, 1118-1128.
30. Z.-N. Xu, J. Sun, C.-S. Lin, X.-M. Jiang, Q.-S. Chen, S.-Y. Peng, M.-S. Wang and G.-C. Guo, *ACS Catal.*, 2013, **3**, 118-122.
31. F. Waller, *J. Mol. Catal.*, 1985, **31**, 123-136.
32. S.-i. Uchiumi, K. Ataka and T. Matsuzaki, *J. Organ. Chem.*, 1999, **576**, 279-289.
33. G. Hong, L. H. Chen, H. Fei and X. G. Hui, *J. Mol. Catal. A: Chem.*, 2005, **235**, 143-149.

34. Y. Ji, G. Liu, W. Li and W. Xiao, *J. Mol. Catal. A: Chem.*, 2009, **314**, 63-70.
35. Q. Lin, Y. Ji, Z.-D. Jiang and W.-D. Xiao, *Ind. & Eng. Chem. Res.*, 2007, **46**, 7950-7954.
36. X. Z. Jiang, Y. H. Su, B. J. Lee and S. H. Chien, *Appl. Catal. A Gen.*, 2001, **211**, 47-51.
37. F. D. Meng, G. H. Xu and Q. R. Guo, *J. Mol. Catal. A: Chem.*, 2003, **201**, 283-288.
38. B. Kalita and R. C. Deka, *Catal. Lett.*, 2010, **140**, 205-211.
39. W. S. A. Halim, M. M. Assem, A. S. Shalabi and K. A. Soliman, *Appl. Surf. Sci.*, 2009, **255**, 7547-7555.
40. K. Honkala, P. Pirilä and K. Laasonen, *Phys. Rev. Lett.*, 2001, **86**, 5942-5945.
41. B. Delley, *J. Chem. Phys.*, 1990, **92**, 508-517.
42. B. Delley, *J. Chem. Phys.* , 2000, **113**, 7756-7764.
43. J. P. Perdew, K. Burke and M. Ernzerhof, *Phys. Rev. Lett.*, 1996, **77**, 3865-3868.
44. J. P. Perdew, K. Burke and M. Ernzerhof, *Phys. Rev. Lett.*, 1997, **78**, 1396-1396.
45. B. Z. Sun, W. K. Chen and Y. J. Xu, *J. Chem. Phys.*, 2010, **133**, 154502.
46. K. N. Ding, X. Z. Xia, X. Lu and J. Q. Li, *Chin. J. Struct. Chem.*, 2013, **32**, 936-948.
47. B. Liu, L. Cheng, L. Curtiss and J. Greeley, *Surf. Sci.* , 2014, **622**, 51-59.
48. Y. Li, Yue Yu, J.-G. Wang, J. Song, Q. Li, M. Dong and C.-J. Liu, *Appl. Catal. B: Environ.*, 2012, **125**, 189-196.
49. L. Versluis and T. Ziegler, *J. Chem. Phys.*, 1988, **88**, 322-328.
50. U. von Barth and L. Hedin, *J. Phys. C: Solid State Phys.*, 1972, **5**, 1629-1642.
51. C.-S. Lee, T.-S. Hwang, Y. Wang, S.-M. Peng and C.-S. Hwang, *J. Phys. Chem.*, 1996, **100**, 2934-2941.
52. Z. G. Wang, Q. D. Zeng, Y. B. Luan, X. J. Wu, L. J. Wan, C. Wang, G. U. Lee, S. X. Yin, J. L. Yang and C. L. Bai, *J. Phys. Chem. B*, 2003, **107**, 13384-13388.
53. T. T. Lin, W.-D. Zhang, J. C. Huang and C. B. He, *J. Phys. Chem. B*, 2005, **109**, 13755-13760.
54. N. Matsuzawa, J. e. Seto and D. A. Dixon, *J. Phys. Chem. A*, 1997, **101**, 9391-9398.
55. I.V. Yudanov, R. Sahnoun, K.M. Neyman, N. Rosch, J. Hoffmann, S. Schauermann, Vi. Joha ´nek, H. Unterhalt, G. Rupprechter, J. Libuda and H.-J. Freund, *J. Phys. Chem. B* 2003, **107**, 255-264.
56. J. R. B. Gomes and F. Illas, *Catal. Lett.*, 2001, **71**, 31-35.
57. J. E. Fieberg and J. M. White, *J. Vac. Sci. & Tech. A*, 1997, **15**, 1674-1678.
58. B. J. Van der Veken, R. Maas, G. A. Guirgis, H. D. Stidham, T. G. Sheehan and J. R. Durig, *J. Phys. Chem.*, 1990, **94**, 4029-4039.
59. M. Aschi and F. Grandinetti, *Chem. Phys. Lett.*, 1996, **258**, 123-128.
60. P. N. Ghosh, A. Bauder and H. H. Günthard, *Chem. Phys.*, 1980, **53**, 39-50.
61. M. Bodenbinder, S. E. Ulic and H. Willner, *J. Phys. Chem.* , 1994, **98**, 6441-6444.
62. C. J. Cassady and B. S. Freiser, *J. Am. Chem. Soc.* , 1985, **107**, 1566-1573.
63. G. Zhenghong, L. Zhongchen, H. Fei and X. Genhui, *Journal of Molecular Catalysis A: Chemical*, 2005, **235**, 143-149.
64. C. M. Grill and R. D. Gonzalez, *J. Phys. Chem.*, 1980, **84**, 878-882.
65. X. L. Shen, Z. M. Chen, Y. Zhao and D. Huang, *Spectrosc. Spect. Anal.*, 2012, **32**, 2946-2949.
66. N. A. Abood, B. A. Saeed and S. M. H. Ismael, *J. Basrah Res. (Sci.)*, 2011, **37**, 93-99.
67. A. Engdahl and B. Nelander, *Chem. Phys. Lett.*, 1988, **148**, 264-268.
68. R. K. HARRIS, *Spectrochimica Acta*, 1964, **20**, 1129-1141.
69. A. R. H. C. a. G. A. OSBORN, *Spectrochimica Acta*, 1971, **27A**, 2461-2490.
70. Q. Lin, Y. Ji, J. Q. Tan and W. D. Xiao, *Chin. J. Catal.*, 2008, **29**, 325-329.

71. L. J. Bellamy, Chapman and Hall, London, 1975.

Schema 1. The pathway network for the reaction of CO and MN. P1 (red, C-C coupling occurs in the third step), P2 (green, C-C coupling occurs in the second step), and P3 (blue, C-C coupling occurs in the first step)

Fig. 1 The optimised stable intermediates formed by CO + OMe and CO + CO co-adsorption on Pd(111). I1: COOMe species; I2: OCCO species. The values in the blue rectangles indicate Mulliken charges. The bond lengths and the adsorption energies are given in Angstroms and kcal/mol. The blue, grey, red, and white balls denote Pd, C, O and H atoms, respectively. The same colour scheme is applied in **Figs. 5-7**.

Fig. 2.DOS of separated components (CO, OMe, and Pd, respectively) before and after adsorption. (a) for I1; (b) for I2.

Fig. 3 (a) IR spectra of CO adsorption on Pd/α-Al_2O_3 at different temperatures; (**b)** CO adsorption of segment of (a). (1)303 K, (2)363 K, (3)403 K, (4)433 K. All In situ infrared acquisition data are first past into the gas, and temperature reach to the specified temperature after balance after 10 min data acquisition.

Fig. 4 (a) IR spectra of CO and MN coupling reaction after CO pre-adsorption on Pd/α-Al_2O_3 at different temperatures; (**b)** CO and MN coupling reaction of segment of (**a**) on the same scale. (1)303 K, (2)363 K, (3)383 K, (4)403 K. All In situ infrared acquisition data are first past into the gas, and temperature reach to the specified temperature after balance after 10 min data acquisition.

Fig.5. The energy profile (P1) for the reaction of CO and MN. All energies are given in kcal/mol.

Fig. 6. The energy profile (P2) for the reaction of CO and MN. All energies are given in kcal/mol.

Fig. 7. The energy profile (P3) for the reaction of CO and MN. All energies are given in kcal/mol.

Fig. 8. Influence of molar ratio of CO to MN on space-time yield of DMO at 403K. (3000 h^{-1}, 50 % N_2 balance, 0.12 MPa)